

Photometry and astrometry with *JWST* – I. NIRCам point spread functions and the first *JWST* colour–magnitude diagrams of a globular cluster

D. Nardiello^{1,2,★}, L. R. Bedin^{1,★}, A. Burgasser³, M. Salaris^{4,5}, S. Cassisi^{5,6}, M. Griggio^{1,7} and M. Scalco^{1,7}

¹*Istituto Nazionale di Astrofisica - Osservatorio Astronomico di Padova, Vicolo dell'Osservatorio 5, I-35122 Padova, Italy*

²*Aix Marseille Univ, CNRS, CNES, LAM, Marseille, F-13007, France*

³*Center for Astrophysics and Space Sciences (CASS), University of California, San Diego, La Jolla, CA 92093, USA*

⁴*Astrophysics Research Institute, Liverpool John Moores University, 146 Brownlow Hill, Liverpool L3 5RF, UK*

⁵*Istituto Nazionale di Astrofisica - Osservatorio Astronomico di Abruzzo, Via M. Maggini, I-64100 Teramo, Italy*

⁶*INFN - Sezione di Pisa, Largo Pontecorvo 3, I-56127 Pisa, Italy*

⁷*Dipartimento di Fisica, Università di Ferrara, Via Giuseppe Saragat 1, I-44122 Ferrara, Italy*

Accepted 2022 September 13. Received 2022 September 13; in original form 2022 August 16

ABSTRACT

As the *James Webb Space Telescope* (*JWST*) has become fully operational, early release data are now available to begin building the tools and calibrations for precision point-source photometry and astrometry in crowded cluster environments. Here, we present our independent reduction of NIRCам imaging of the metal-poor globular cluster M 92, which were collected under Director's Discretionary Early Release Science programme ERS-1334. We derived empirical models of the point spread function (PSF) for filters *F090W*, *F150W*, *F277W*, and *F444W*, and find that these PSFs: (i) are generally undersampled (FWHM ~ 2 pixel) in *F150W* and *F444W* and severely undersampled (FWHM ~ 1 pixel) in *F090W* and *F277W*; (ii) have significant variation across the field of view, up to ~ 15 – 20 per cent; and (iii) have temporal variations of ~ 3 – 4 per cent across multi-epoch exposures. We deployed our PSFs to determine the photometric precision of NIRCам for stars in the crowded, central regions of M 92, measured to be at the ~ 0.01 mag level. We use these data to construct the first *JWST* colour–magnitude diagrams of a globular cluster. Employing existing stellar models, we find that the data reach almost the bottom of the M 92 main sequence ($\sim 0.1 M_{\odot}$), and reveal 24 white dwarf candidate members of M 92 in the brightest portion of the white dwarf cooling sequence. The latter are confirmed through a cross-match with archival *HST* UV and optical data. We also detect the presence of multiple stellar populations along the low-mass main sequence of M 92.

Key words: techniques: image processing – techniques: photometric – stars: Population II – white dwarfs – globular clusters: individual: NGC 6341 (M 92).

1 INTRODUCTION

In the past 30 yr, space telescopes have revolutionized the world of astronomy, with new and, sometimes, unexpected discoveries. Notable examples include *Hipparcos* (Høg et al. 2000) and *Gaia* (Gaia Collaboration 2016), which significantly advanced the field of astrometry and contributed to our understanding of stellar astrophysics and Milky Way structure; *Kepler* (Borucki et al. 2010) and *TESS* (Ricker et al. 2015), whose precision light curves greatly expanded the fields of exoplanets and variable stars; *Spitzer* (Werner et al. 2004), *Herschel* (Pilbratt et al. 2010), and *WISE* (Wright et al. 2010), whose sensitivity at infrared (IR) wavelengths advanced studies of star-forming regions, distant galaxies, and cosmology; and *Chandra* (Weisskopf et al. 2002) and *XMM–Newton* (Jansen et al. 2001), which enabled X-ray observations of the most energetic

phenomena in the near and distant Universe. Arguably the most successful and longest lived of the space observatories has been the *Hubble Space Telescope* (*HST*), whose instruments enable UV, optical, and infrared imaging and spectroscopy at high spatial resolution and sensitivity, and continues to provide revolutionary results in all areas of astrophysics.

On 2021 December 25, the NASA/ESA/CSA *James Webb Space Telescope* (*JWST*; Gardner et al. 2006) was successfully launched on an Ariane 5 rocket from the Guiana Space Centre in Kourou, French Guiana. Over the subsequent six months after arrival, *JWST* successfully passed all phases of commissioning and testing, and on 2022 July 11 the first science images from the facility were made public. *JWST*'s 6.5 m primary mirror is formed by 18 hexagonal mirror segments made of gold-plated beryllium, which allow the telescope to observe at both near-IR and mid-IR wavelengths (0.6–28.3 μm). Four science instruments (NIRCам, NIRSpec, MIRI, and NIRISS) and a guide camera (FGS) are mounted in the Integrated Science Instrument Module. Their varied capabilities are enabling analysis

* E-mail: domenico.nardiello@inaf.it (DN); luigi.bedin@inaf.it (LB)

of the light of the first galaxies, the study of exoplanet atmospheres, and improved understanding of the origins and evolution of resolved stellar populations in clusters and nearby galaxies (Greene et al. 2019; Meixner et al. 2019; Rieke et al. 2019; Windhorst et al. 2019).

Before the launch of *JWST*, 13 Director's Discretionary Early Release Science (DD-ERS) programmes¹ were selected to conduct the first scientific observations with the facility after the completion of commissioning. These data are immediately released to the public.

This is the first in a series of papers aimed at exploring the astrometric and photometric capabilities of *JWST*'s instruments based on data collected during the DD-ERS programmes, with the goal of developing the tools needed to obtain high-precision photometry and astrometry of stars in crowded environments. In this work, we extract effective point spread functions (PSFs) and photometry for stars in the very metal poor globular cluster NGC 6341, based on images collected with the Near Infrared Camera (NIRCam) of *JWST* as part of programme ERS-1334 (PI: Weisz). Subsequent works will focus on correcting geometric distortion and obtaining precision astrometry of stars with NIRCam (Paper II, Griggio et al. in preparation), analysis of resolved galaxies (Paper III, Bedin et al. in preparation), and on the use of the NIRISS and FGS images for crowded field studies (Paper IV, Nardiello et al. in preparation). This article is structured as follows: Section 2 describes the NIRCam observations presented in this work. Section 3 reviews the procedures used to derive effective PSF models for each of the four NIRCam filters used, and to extract the first *JWST* photometric catalogues of stars in M 92. Section 4 reports the procedures used to transform instrumental magnitudes into a photometric system defined by theoretical models. Section 5 describes an analysis of the M 92 colour–magnitude diagrams (CMDs) obtained by combining *JWST* and *HST* imaging data. Section 6 summarizes our conclusions.

2 OBSERVATIONS

The NIRCam imaging camera covers the red optical and near-IR wavelength range 0.6–5 μm in two simultaneous channels: the short wavelength (SW) channel (0.6–2.3 μm) and the long wavelength (LW) channel (2.4–5.0 μm). Each channel consists of two modules (A and B) that operate in parallel. The field of view of each module is 2.2×2.2 (4.84 arcmin²), and these are separated by a gap of ~ 44 arcsec. The total field of view for each channel is about 9.7 arcmin². In the SW channel, gaps of ~ 5 arcsec separate the four detectors that constitute each module. Both modules in each channel operate with the same set of narrow-, medium-, and wide-band filters. The imaging resolution for the SW channel is ~ 31 mas per pixel, while for the LW channel it is ~ 63 mas per pixel.

DD-ERS programme ERS-1334 used NIRCam to image NGC 6341 (M 92), a very metal poor globular cluster ([Fe/H] = -2.3 , Harris 1996) located at a distance of ~ 8.5 kpc from the Sun. Observations were obtained over 2022 June 20–21 for a total 1.95 h, using filters *F090W* ($\lambda \sim 0.8$ –1.0 μm) and *F150W* ($\lambda \sim 1.3$ –1.7 μm) in the SW channel, and *F277W* ($\lambda \sim 2.4$ –3.1 μm) and *F444W* ($\lambda \sim 3.9$ –5.0 μm) in the LW channel. For each filter, four exposures of 311.37 s each were obtained using the, SHALLOW4 readout mode (4 frames averaged and 1 frame skipped), for a total integration time of 1245.48 s per filter. These images were obtained in a 4-point sub-pixel dither pattern to mitigate cosmic rays, bad pixels, and improve the sampling of the PSF. Both NIRCam channels were centred such that the 44 arcsec gap between the modules covered the centre

of the cluster, as illustrated in the stacked, three-colour (*F090W*, *F150W*, and *F444W*) image shown in Fig. 1.

For our analysis, we used the single exposure calibrated images (`.cal`) that are created by the Stage 2 pipeline `calwebb_image2`.² Each pixel is calibrated by the pipeline to units of MJy per steradian. We converted these values into counts by using the header keywords PHOTMJSR (flux density in MJy per steradian corresponding to 1 count per second) and XPOSURE (effective exposure time). We also used the Data Quality (DQ) image included in the `.cal` fits data cube to flag bad and saturated pixels on the science image.

A total of $8 \times 2048 \text{ pixel} \times 2048 \text{ pixel}$ images are associated with each exposure obtained with the SW channel (four images for each module), while $2 \times 2048 \text{ pixel} \times 2048 \text{ pixel}$ images are associated to each exposure obtained with the LW channel (one for each module). We excluded from our reduction and analysis the `.cal` exposures with root-name `jw01334001001.02101.00003` (involving filters *F090W* and *F277W*, for a total of 10 images) as they were found to be unusable. We therefore reduced 24, 32, 6, and 8 images in *F090W*, *F150W*, *F277W*, and *F444W* filters, respectively.

3 PSF MODELLING AND DATA REDUCTION

As reported in the *JWST* documentation,³ the NIRCam PSFs (in imaging mode) are Nyquist sampled for wavelengths longer than 2.0 μm in the SW channel and 4.0 μm in the LW channel, corresponding to full-width at half-maximum FWHM ~ 2 –3 pixels. At shorter wavelengths, the PSFs are under-sampled. Deriving a correct model for an undersampled PSF is a challenging but necessary task, as incorrect PSFs can introduce systematic errors in the extraction of positions and fluxes of stars (Anderson & King 2000).

We followed the empirical approach developed by Anderson & King (2000, hereafter AK00) for the *HST* Wide-Field Planetary Camera 2 (WFPC2) to obtain a model of the *effective* pixel-convolved PSF (ePSF). This approach has been used to derive ‘library’ (reference) ePSFs for the *HST* Advanced Camera for Survey (ACS; Anderson & King 2004, 2006) and the Wide Field Camera 3 (WFC3; Anderson et al. 2015; Anderson 2016), which to this day represent the state of the art for point-source photometry and astrometry. The ePSF approach has also been applied to the modelling of under-sampled PSFs in Kepler/K2 images (Nardiello et al. 2016; Libralato et al. 2016a,b). The procedure outlined below was applied independently for each set of images in a given detector/filter combination.

To break the degeneracy between position and flux of a source (see fig. 1 of AK00) to derive a well-sampled PSF model, it is necessary to precisely constrain the positions and fluxes for a set of stars. However, this information can not be obtained accurately if the PSF is not appropriately modelled. As such, an iterative approach is required: starting from a first-guess catalogue of positions and fluxes of isolated, bright, unsaturated point sources, we alternately derive the ePSF model and the stars’ positions and fluxes, improving at each iteration both sets of quantities until reasonable convergence is achieved.

3.1 A first-guess catalogue of stars

For each image, we first extracted a initial estimate of the empirical PSF following the approach by Anderson et al. (2006). PSFs models

¹<https://www.stsci.edu/jwst/science-execution/approved-ers-programs>

²<https://jwst-pipeline.readthedocs.io/>

³<https://jwst-docs.stsci.edu/>



Figure 1. Three-colour stacked image of the NIRC2 field of view centred on M 92. The filters $F444W$, $F150W$, and $F090W$ have been used for the red, green, and blue channels, respectively. The field is oriented with North up and East left. In the $F444W$ stacked image, we masked pixels corresponding to the gaps of the SW channel.

are obtained for each image in a total empirical way, by normalizing a sample of isolated, bright stars for their total flux, and averaging them on a grid of 201×201 points defined in a space that supersamples the PSF pixel by a factor 4. These empirical PSFs, even if already good enough for measuring with a first approximation the positions and the fluxes of the stars, are not sufficient for high-precision photometric and astrometric measurements of the stars, particularly in crowded environments. We then used these initial PSFs to measure the positions and fluxes of isolated (the peak must be at least 10 pixels from the nearest peak), bright (the minimum flux above the local sky must be at least 3000 counts), unsaturated stars in each image. In this step we used the software `img2xym`, developed by Anderson et al. (2006) for the Wide Field Imager (WFI) @ ESO/MPG 2.2m telescope, and adapted to NIRC2 data. This algorithm finds, models, measures, and subtracts stars that are progressively fainter through an iterative process, simultaneously fitting the positions and fluxes of each star and its (potentially overlapping) neighbours. We cross-identified the stars in each image in a given detector/filter dither set, then transformed the positions and fluxes of the stars into a single catalogue anchored to a common reference system associated to the first image in each set, using six-parameter linear transformations and photometric zero-point shifts. The transformed positions and fluxes of each star detected in at least three images are then used to define a master catalogue that serves as the reference for modelling the ePSF model for a given detector and filter. Each catalogue contains between 1500 and 6000 stars depending on the channel, module, detector, and filter it represents.

3.2 Obtaining the effective point spread function

Given an individual star centred at (x_*, y_*) and having flux f_* , every pixel (i, j) of an image close to the star samples the normalized ePSF

ψ as

$$\psi(\Delta x, \Delta y) = \frac{P_{i,j} - s_*}{f_*}, \quad (1)$$

where $P_{i,j}$ is the count value of the image at pixel (i, j) , $(\Delta x, \Delta y) = (i - x_*, j - y_*)$ is the pixel offset from the star's centre, and s_* is the local sky background, measured as the mode of the pixel value distribution computed in an annulus of radii $r_{in} = 7$ pixel and $r_{out} = 13$ pixel and centred on the star. Knowing the flux and position of each star in each exposure, each pixel (i, j) close to the star represents a sampling of the PSF at one point in the 2D array that defines the ePSF.

Our procedure to determine an overall ePSF model followed these steps (we refer the reader to AK00 for a more detailed description of these steps):

(i) We first transformed the positions of the stars in the master catalogue on to the reference system of each individual image using the transformations described above.

(ii) We then converted each pixel value within 10 pixels of the star's centre in a given image into an estimate of the corresponding point in the ePSF model. Given the large number of stars in each master catalogue, there are of order millions of point sampling used to determine the ePSF model.

(iii) The ePSF model was constructed by projecting these individual point samplings from the $10 \text{ pixel} \times 10 \text{ pixel}$ original image scale to a finer ePSF grid super-sampled by a factor of 4 ($41 \text{ points} \times 41 \text{ points}$). In the 1st iteration, each ePSF grid-point was calculated as the 2.5σ -clipped average of point sampling within a square of 0.25 pixels in Δx and Δy coordinates. In subsequent iterations, we first subtracted from each sampling the corresponding value in the current ePSF model, then calculated the 2.5σ -clipped average of the residuals in each $0.25 \text{ pixel} \times 0.25 \text{ pixel}$ grid point. This residual

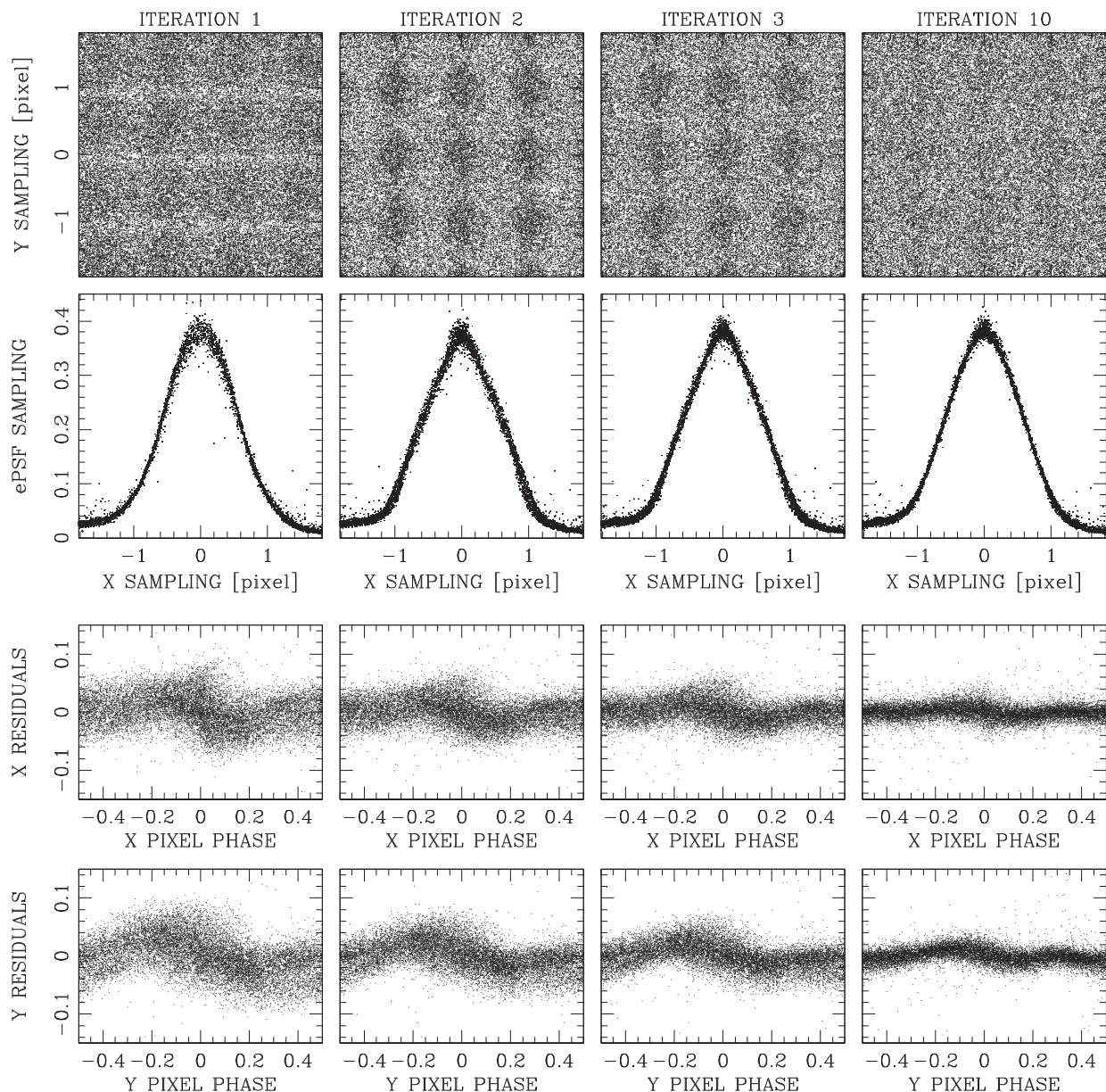


Figure 2. Overview of the iterative process to determine the ePSF model for filter *F090W* for detector 4 of module A, in the case of no spatial variation of the PSF across the field of view. The top row shows the location of the estimated value of the ePSF with respect to the centre of the stars (0,0), i.e. the ePSF *x/y* sampling; only 2.5 percent of the points are plotted. The second row displays the ePSF *x* sampling for a slice across the centre of the ePSF with $|\delta y| < 0.05$. The bottom two rows illustrate the pixel-phase errors along the *x* and *y* axes, respectively. From left to right, the panels correspond to iterations 1, 2, 3, and 10.

grid was then added to the last available ePSF model, and the result was smoothed with a combination of quadratic and quartic kernels, re-centred, and re-normalized;

(iv) Using the updated ePSF model, we remeasured the positions and fluxes of stars in the master catalogue in each image; then transformed the positions back to the original reference frame and computed average fluxes to update the catalogue.

We performed this iterative process ten times, assuming a single ePSF model (no spatial variation). Fig. 2 shows the improvement of the ePSF model from the first iteration to the tenth iteration. In the first iteration, the point samplings are not homogeneously distributed, and the ePSF shape has significant scatter among the samples. As the ePSF model improves, both the point samplings and scatter in the ePSF profile improve. The improvement of the

ePSF model can be particularly discerned in the distribution of pixel phase errors, i.e. the difference between the expected positions (transformed from the master catalogue to each individual image) and the measured positions of the stars (obtained using the ePSF model at each iteration), as a function of the pixel phase.⁴ This distribution shows a sinusoidal pattern in the first iteration, expect for an offset ePSF model; this pattern flattens as the ePSF model improves.

After the tenth iteration, we saw no improvement in the pixel phase error distribution or sample scatter in ePSF model. However, PSFs

⁴Specifically, the pixel phase of a star, defined as $\phi_x = x - \text{int}(x + 0.5)$ and $\phi_y = y - \text{int}(y + 0.5)$, is the location of the star with respect to the pixel boundaries.

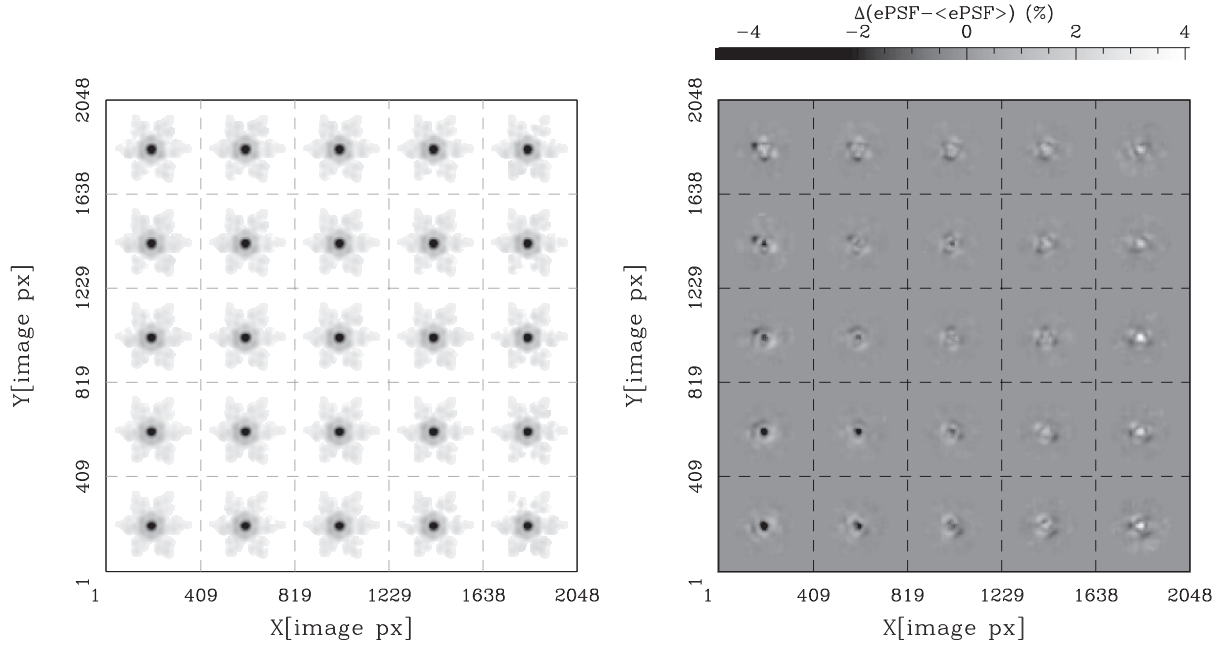


Figure 3. Overview of the spatial variation of the ePSF model for filter *F150W* and detector 1 of module A in the SW channel. The left panel shows the final 5×5 array of ePSFs calculated in image sub-regions of size 409 pixel \times 409 pixel. The right-hand panel shows the difference between each ePSF and an average of all 25 ePSFs across the detector. The scale of the variation compared to the normalized ePSF is indicated by the colour bar above the panel.

vary with location across the detector due to projection effects, so subsequent iterations of this process introduced a spatial variation to the ePSF model. This variation was done by dividing the image into sub-regions, then calculating the ePSF model in each of these regions following the steps above, starting with the ‘global’ ePSF model calculated at the end of the tenth iteration. We increased the number of sub-regions in stages, starting with 2×2 sub-regions of dimension 1024 pixel \times 1024 pixel (iterations 11–13), then 3×3 sub-regions of dimension 682 pixel \times 682 pixel (iterations 14–16), and finally 5×5 sub-regions of dimension 409 pixel \times 409 pixel (iterations 17–21). Fig. 3 shows an example of the final ePSF array for filter *F150W* and detector 1 of module A in the SW channel. The peak-to-peak variation is about 9 percent in this case, while maximum variations of up to 15–20 percent were found for the ePSF arrays in *F090W* images.

3.3 Time variability of the ePSF

If the library ePSF model determined above is constant in time, it could in principle be used to derive the positions and fluxes of stars in all images obtained with NIRCcam. However, past experience with *HST* shows that, even in ideal and stable conditions, PSFs are known to vary with time.

In order to measure and minimize the effects of time variation of the ePSF model, we performed a perturbation analysis originally introduced in Anderson & King (2006) (see also Anderson et al. 2008) and deployed in several subsequent *HST* works (e.g. Nardiello et al. 2018). Briefly, for a given detector/filter set, we start with the library ePSF measured from an initial data-set (in this case, the M 92 observations), and perturb it to account for ePSF variations that emerge in a second data set. For the latter, we used NIRCcam observations of the Wolf-Lundmark-Melotte (WLM) irregular galaxy (Wolf 1909; Melotte 1926; Holmberg 1950), also obtained in programme ERS 1334 about one month after the M 92

observations.⁵ We follow a similar iterative procedure as outlined above. We started by using the initial library ePSF model to measure the positions and fluxes of a set of bright, unsaturated, isolated stars in the second data set. We then subtracted the ePSF models from these stars, and re-sampled the residuals on to a grid of residuals, that will be used to perturb the original library ePSFs. The spatial grid of mean residual can vary from 1×1 to 5×5 (same grid as the ePSFs) based on the number of stars available in the field of view of the image (minimum 15 stars in a sub-region). Each point of the grid corresponds to a point of the image, and, when the used grid is smaller than 5×5 , we used bi-linear interpolations to calculate the perturbation to add to each of the 25 library ePSFs. We repeated this procedure five times to converge to an optimally perturbed ePSF model grid.

Fig. 4, demonstrates the results of the library ePSF perturbation. The 5×5 residual array between the M 92 ePSF model and final WLM ePSF model shows variations of order 3–4 per cent, indicating that temporal variations of the NIRCcam PSF are significant: the left-hand panel shows the residuals we added to the library ePSF calculated iteratively modelling and subtracting the stellar models on a grid of 5×5 residual points. On the right we illustrate how the quality-of-fit (qfit) diagnostic,⁶ which assess the quality of a PSF model fit to an individual star (the smaller is the qfit, the better the

⁵We specifically evaluated the image jw01 3340 050 01.02101.00001.nrcb3.cal, corresponding to channel SW, module B, detector 3, and filter *F090W*.

⁶The quality-of-fit parameter describes the mean difference between the real star and the model, and it is defined as $\text{qfit} = \sum_{i,j} (P_{i,j} - f_* \times \psi) / \sum_{i,j} P_{i,j}$, where $i = x_0 - 5, \dots, x_0 + 5$, $j = y_0 - 5, \dots, y_0 + 5$, (x_0, y_0) is the star centre, $P_{i,j}$ is the value of the pixel in (i, j) , f_* is the total flux of the star from the PSF fitting, and ψ is the PSF model.

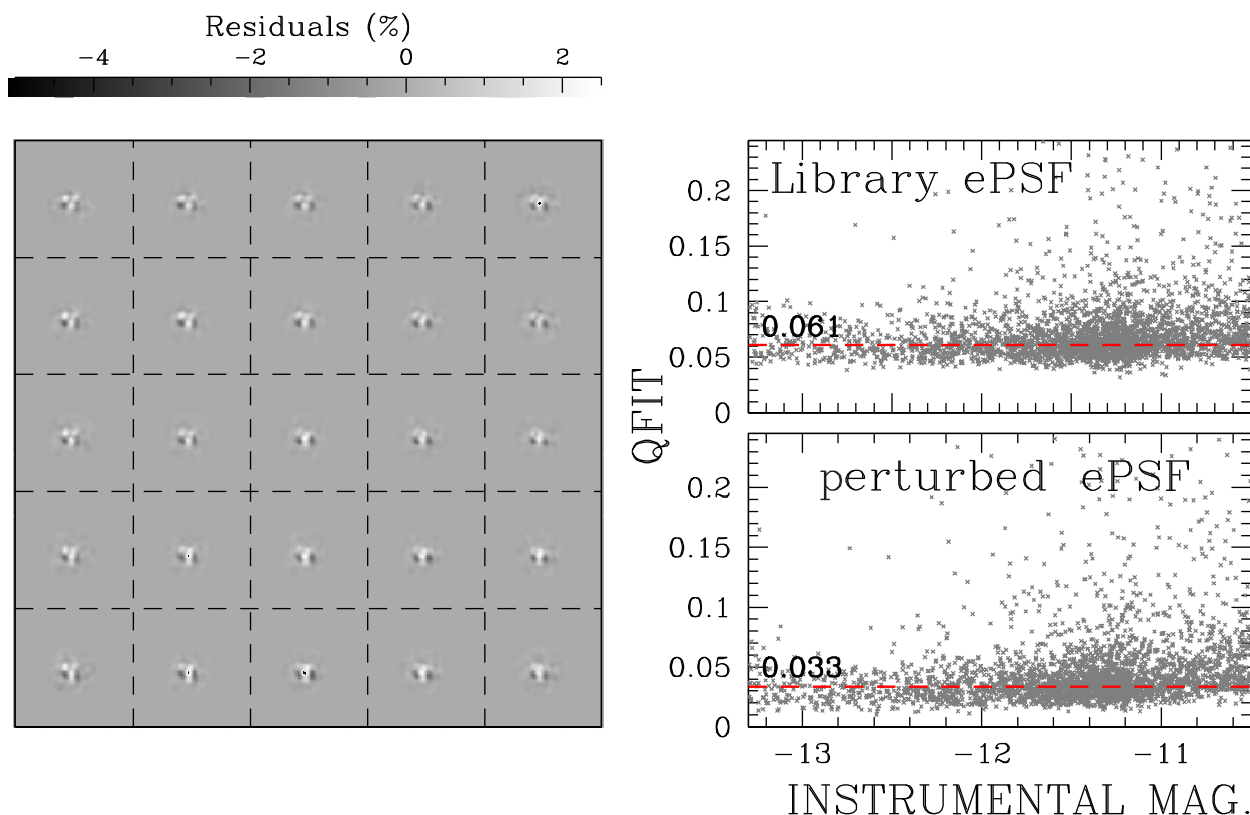


Figure 4. Overview on the results obtained from library ePSF perturbation from our M 92 ePSF grid to observations of the WLM galaxy, also obtained with NIRC*am*. The left-hand panel shows the residuals added to the library ePSFs to obtain the perturbed ePSFs. The total variation across the grid goes from ~ -4 per cent to ~ 2 per cent. The right-hand panel shows the quality-of-fit (qfit) as a function of instrumental magnitude before (top panel) and after (bottom panel) perturbation of the library ePSF. The median qfit for bright stars (instrumental magnitude between -13.0 and -10.5) declines from ~ 0.06 to ~ 0.03 .

PSF fit), improves significantly after the perturbation of the library ePSFs.

We conclude that, when possible based on the number of available bright stars, perturbation of the library ePSFs such as those presented here are necessary to achieve the best photometric (and presumably astrometric) measurements.

3.4 M 92 data reduction

With the library of ePSF model arrays determined for the full set of filters and detectors in our data set, we extracted the positions and fluxes of stars in each individual image adopting the PSF-fitting software *img2xym*, already used and described in Section 3.1. We set a faint limit for source detection (local maxima above the neighbouring sky) as an integrated flux of at least 50 counts, and at least five pixels from the closest source.

We cross-matched and transformed all source positions on to a common reference system to derive a final catalogue of stars across each image dither set. Because the exposures are dithered by only a few tens of pixels, individual detectors do not overlap. We therefore analysed detector and filter combinations individually, generating separate catalogues for each. Sources were required to be detected in at least three images. Each catalogue includes the reference pixel positions of the stars, their instrumental magnitudes⁷ and uncertainties, and the mean qfit.

⁷The instrumental magnitude is defined as $m_{\text{INSTR}} = -2.5 \times \log f_{\text{PSF}}$, where f_{PSF} is the total flux of the star (in counts) measured through PSF fitting.

We purged these catalogues of bad detection, PSF artefacts, and other contaminants by using the procedures described in Nardiello et al. (2018) and illustrated in Fig. 5. Specifically, we used both photometric errors as a function of instrumental magnitude and the qfit statistic to identify and remove non-stellar sources. Fig. 5 also shows the instrumental $F090W$ versus $F090W-F150W$ CMD before and after this cleaning procedure. It is important to note that this CMD includes sources not only clearly detectable in individual images, but present in at least 3 out of 4 images. As such, these preliminary CMDs do not go as faint as the data would allow, and are probably rather incomplete. Moreover, derived photometry are still vulnerable to pixel-area effects, these due to geometric distortion, to lithographic effects (e.g. Anderson & King 1999; Bellini, Anderson & Bedin 2011), or to both. Future work will address these issues.

4 PHOTOMETRIC REGISTRATION

As a first attempt at calibrating the instrumental magnitudes of the stars detected in the M 92 observations, we cross-matched our catalogues with the *.cat* outputs of the Stage 3 pipeline *cal-webb_image3*, based on pre-flight data. However, when comparing the CMDs obtained for stars on different detectors and modules, it was clear that there were significant photometric zero-point offsets, up to 0.4 mag. There were also significant deviations in overlapping CMDs obtained matching the *JWST.cat* catalogues with the publicly available *HST* catalogue of M 92 released by

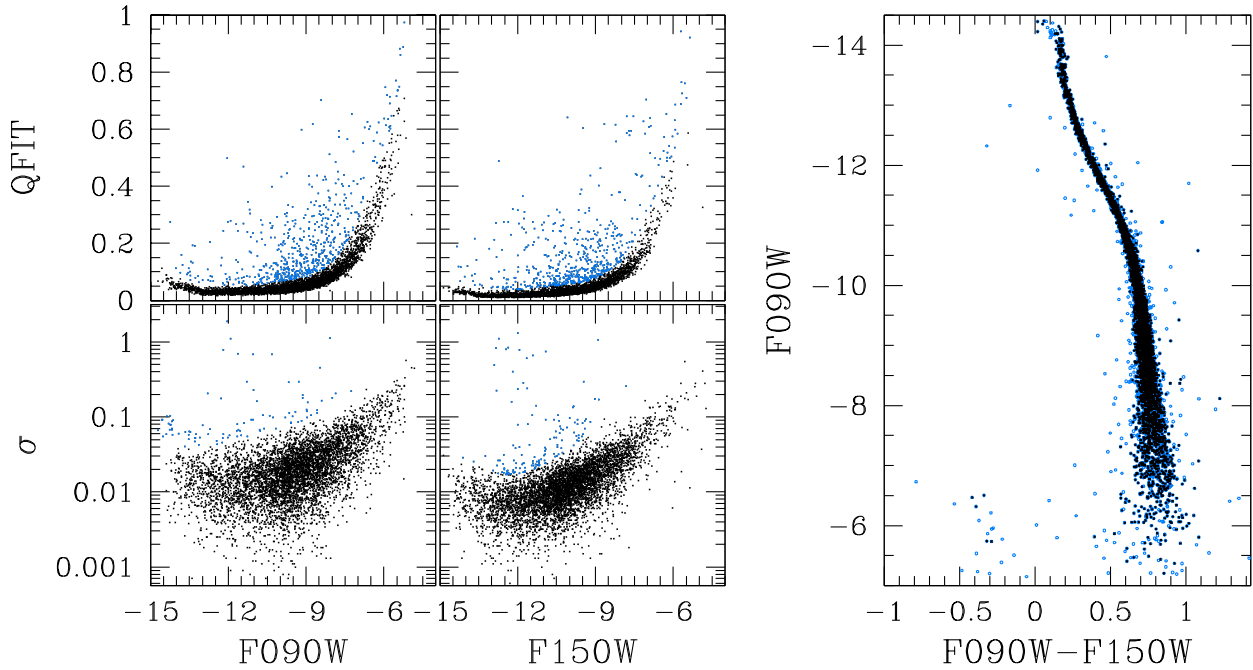


Figure 5. Procedure adopted for rejecting bad detection and measurements in point-source photometry. The left-hand panels show the selections performed in the photometric error (bottom panels) and qfit distributions (top panels) for the *F090W* (left) and *F150W* (right) filters; azure points indicate rejected sources. The right-hand panel shows the instrumental *F090W* versus *F090W*–*F150W* CMD for well-measured (black) and rejected sources (azure). This CMD is based on the final source catalogues for images obtained with detector 1 of module A in the SW channel.

the ‘*HST* UV Globular cluster Survey’ (HUGS;⁸ Nardiello et al. 2018), based on data collected under *HST* programmes GO-10775 (PI: Sarajedini, Sarajedini et al. 2007) and GO-13297 (PI: Piotto, Piotto et al. 2015). These photometric offsets have been also observed by other teams (e.g. the research note by Boyer et al. 2022, or the zero-point corrections tabulated by G. Brammer).⁹ The photometric offsets are correlated to the absolute flux zero-points adopted by the *JWST* pipeline to calibrate the single detectors. Actually, the *JWST* calibration programmes are still ongoing, and the zero-points used in the calibration pipeline are still far to be perfect. We therefore pursued an alternative approach, bootstrapping the *JWST* measurements to the *HST* data and theoretical models.

We first measured the distance of M 92 by comparing the *HST* m_{F606W} versus $m_{F606W} - m_{F814W}$ CMD with the BASTI-IAC models (Hidalgo et al. 2018; Pietrinferni et al. 2021). For the models, we assumed an age $\tau = 13.0$ Gyr, metallicity $[\text{Fe}/\text{H}] = -2.31$, and alpha enrichment $[\alpha/\text{Fe}] = +0.4$ (Harris 1996). We selected the stars in magnitude interval $16.5 \leq m_{F606W} \leq 20.5$, roughly ± 2 mag around the main sequence (MS) turn-off (TO). We determined the fiducial line of these stars by using a naive estimator. We divided the MS and red giant branch (RGB) sequences into bins of $\delta m_{F606W} = 0.5$ mag, and in these intervals defined a grid of N points separated by steps of width $\delta m_{F606W}/4$. In each interval $m_{F606W}^i < m_{F606W} < m_{F606W}^{i+1}$, with $i = 1, \dots, N$, we calculated the median colour and magnitude of the stars within the magnitude interval. We then interpolated these median points using a cubic spline (for a more detailed description of this procedure, see Nardiello et al. 2015; Lucertini, Nardiello & Piotto 2021). We then calculated the χ^2 between the fiducial line and the

isochrone model, shifted by a grid of distance moduli and reddening values, and determined a minimum χ^2 for a distance modulus $(m - M)_0 = 14.65 \pm 0.07$ ($d = 8.51 \pm 0.28$ Kpc) and reddening $E(B - V) = 0.02 \pm 0.01$ (see Fig. 6). These values are in agreement with measurements previously reported in the literature (Baumgardt & Vasiliev 2021 and references therein).

To register the photometry of stars in the *JWST* catalogues, we cross-matched these with sources in the *HST* HUGS catalogue of M 92. We then generated m_{F606W} versus $m_{F606W} - X$ CMDs, where the X represents uncalibrated photometry in each of the NIRCcam filters *F090W*, *F150W*, *F227W*, and *F444W*. We then calculated fiducial lines in a range of magnitudes $19.5 \leq m_{F606W} \leq 22.5$, along the MS, following the procedure described above. Shifting the m_{F606W} versus $m_{F606W} - X$ model isochrone on to the observational plane using the distance modulus and reddening computed above, we calculated the mean difference between the colour of the fiducial line and the shifted isochrone. This value represents the photometric zero-point needed to bring instrumental magnitudes from each detectors on to a common photometric VEGAMAG reference system defined by the BASTI-IAC models for the assumed cluster parameters (reddening, distance, $[\text{Fe}/\text{H}]$, $[\alpha/\text{Fe}]$, etc). The registration procedure is illustrated in Fig. 7 for the case of *F090W* data from detector 1 of module A in the SW channel. Table 1 summarizes the zero-points we determined for all of the detectors and filters, with uncertainties taking into account contributions from the uncertainties on the photometry, reddening, and distance modulus. The offsets between the different photometric zero-points are in agreement, within the errors, with those tabulated online by G. Brammer.

For channel LW, which has only a single detector per module, we evaluated the possibility of spatial variation of the photometric zero-point across the field of view of each module as follows. We first

⁸<https://archive.stsci.edu/prepds/hugs/>

⁹<https://github.com/gbrammer/grizli/pull/107>

Table 1. Photometric zero-points to bring instrumental magnitudes from different detectors on to a common photometric reference system consistent with models by BASTI-IAC for the assumed cluster parameters determined from optical *HST* data.

SW channel					
Detector	<i>F</i> 090W	<i>F</i> 150W	Detector	<i>F</i> 090W	<i>F</i> 150W
A.1	32.23 ± 0.03	31.88 ± 0.03	B.1	32.10 ± 0.03	31.84 ± 0.04
A.2	32.20 ± 0.04	31.89 ± 0.04	B.2	32.08 ± 0.04	31.83 ± 0.04
A.3	32.20 ± 0.04	31.86 ± 0.05	B.3	32.11 ± 0.05	31.85 ± 0.05
A.4	32.28 ± 0.05	31.98 ± 0.06	B.4	32.17 ± 0.06	31.95 ± 0.06
LW Channel					
Module	<i>F</i> 277W	<i>F</i> 444W	Module	<i>F</i> 277W	<i>F</i> 444W
A	31.01 ± 0.07	30.28 ± 0.07	B	31.12 ± 0.06	30.34 ± 0.07

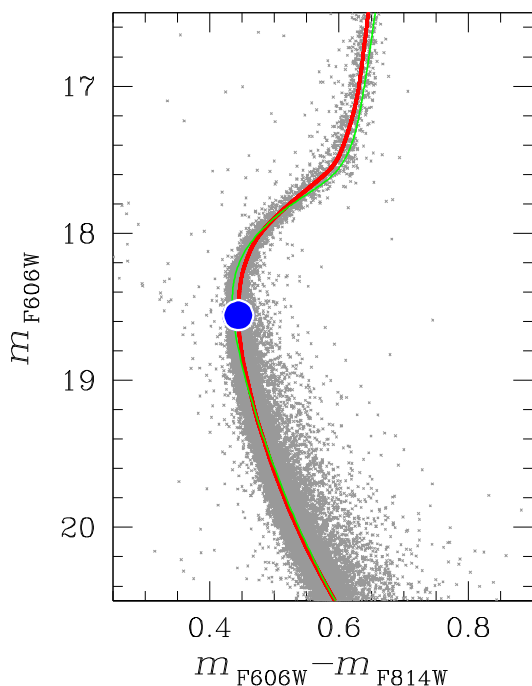


Figure 6. The main sequence turnoff region (blue point) of M 92 in the *HST* m_{F606W} versus $m_{F606W} - m_{F814W}$ CMD. The fiducial line is plotted in red, while the green line traces the 13 Gyr BASTI-IAC isochrone, shifted to match the observed CMD by adjusting the distance modulus and reddening as determined in this work (see text for details).

divided each module into four regions of 1024 pixel \times 1024 pixel, and matched the *F*277W and *F*444W catalogues corresponding to these regions to the *F*090W catalogues.¹⁰ We then calculated zero-point corrections for each region by comparing the theoretical models and fiducial lines as described above. We found that the zero-point correction does vary by $\sim \pm 0.05$ mag between regions, indicating that such a correction is necessary for high-precision photometry. This is approximately the same order of variation among the zero-points in each of the individual SW detectors within a given module.

¹⁰We could not use the *HST* catalogues for this correction because about half of the field of view of each module is outside the field of view of the *HST* images

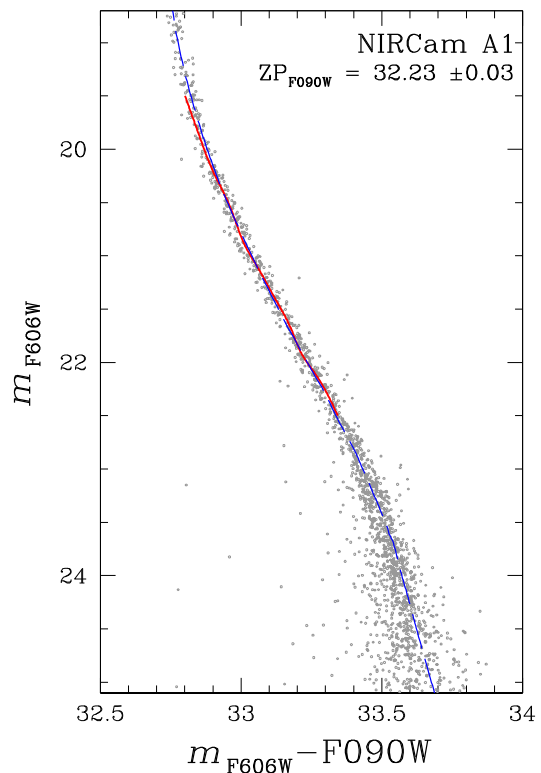


Figure 7. Photometric calibration of data from filter *F*090W of detector 1 of module A in the SW channel. Grey points are the m_{F606W} versus $m_{F606W} - F090W$ CMD (where *F*090W is uncalibrated instrumental magnitudes). The red line represents the fiducial line of the CMD. The dashed blue line is the 13 Gyr BASTI-IAC isochrone, shifted by the distance modulus and reddening values determined in this work, and offset by the desired *F*090W photometric zero-point.

5 COLOUR-MAGNITUDE DIAGRAMS OF M 92

With the individual zero-points calibrated, we can now evaluate the infrared CMDs of M 92 revealed by the *JWST* data. Fig. 8 compares six CMD combinations derived by combining all the *JWST* catalogues extracted in this work. We superimposed to these CMDs the BASTI-IAC isochrone models used to calibrate the zero-points. We find that all of the CMDs reach down to or below the faint end of the MS locus, at least to a stellar mass of about 0.1 M_{\odot} . The CMD that reaches the bottom of the MS with the highest signal-to-noise ratio (S/N) is m_{F090W} versus $m_{F090W} - m_{F150W}$. Indeed, at $m_{F090W} \sim 26$, we measure an S/N ~ 12 in *F*090W and S/N ~ 20 in *F*150W, while

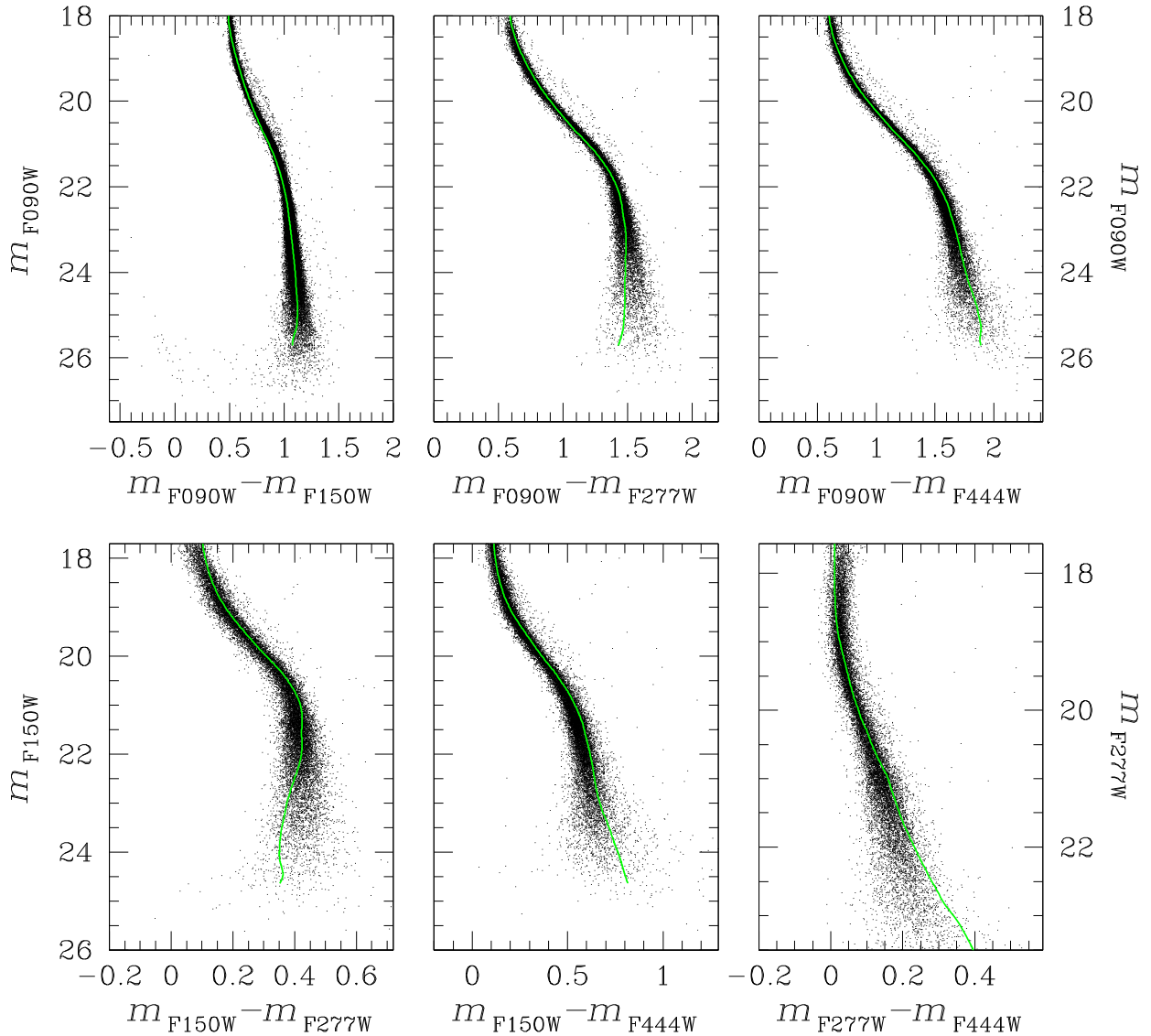


Figure 8. Colour–magnitude diagrams inferred from the calibrated *JWST* data. The green lines are the BASTI-IAC 13 Gyr isochrone.

for stars at the equivalent *F090W* magnitude the LW measurements have $S/N \sim 10$ for *F277W* and $S/N \sim 8$ for *F444W*.

5.1 M92 White dwarfs

In the m_{F090W} versus $m_{F090W} - m_{F150W}$ CMD, we identified 24 sources that passed the quality selection criteria at magnitudes $m_{F090W} \gtrsim 23$ and colour $(m_{F090W} - m_{F150W}) \lesssim 0.3$. We visually confirmed that these sources correspond to robust point-sources in the stacked *F090W* and *F150W* frames (Fig. A1 in Appendix A). These stars are likely white dwarfs (WDs) in M 92. To verify this hypothesis, we first cross-matched the *F090W* and *F150W* catalogues with *F225W* and *F275W* UV catalogues generated by reducing *HST* data collected in programme GO-15173 (PI: Kalirai). Fig. 9 displays the resulting CMDs. We found seven WD candidates were matched between *JWST* and *HST* data sets, and all of them lie on the WD sequence in the m_{F225W} versus $m_{F225W} - m_{F275W}$ CMD. We also compared both IR and UV CMDs of the WD cooling sequence with two $0.54 M_{\odot}$ cooling tracks with hydrogen and helium atmospheres from the BaSTI-IAC database (Salaris et al. 2022). We are observing the bright part of

the WD cooling sequence of M 92 in the *JWST* catalogues, where the mass of the evolving WDs is practically constant and equal to $\sim 0.53 \pm 0.01 M_{\odot}$ (Kalirai et al. 2009). The excellent alignment of the selected sources with the theoretical cooling tracks in both IR and UV CMDs confirms their WD nature. Paper II will calibrate with the geometric distortion of NIRCcam, making possible proper motions measurements for those sources in common with *HST* collected between 3 and 20 yr earlier, which will confirm or refute the membership of these WDs in M 92.

5.2 Multiple populations in M 92

Like almost all the old Galactic globular clusters (e.g. Piotto et al. 2015; Bastian & Lardo 2018) and extragalactic globular clusters (e.g. Larsen et al. 2014; Nardiello et al. 2019), M 92 hosts multiple stellar populations characterized by different light element (C, N, O, Al, Mg, etc) and helium abundances. Analysis by Milone et al. (2017) indicates that M 92 hosts at least three different stellar populations: a ‘first generation’ (1P) having primordial helium content and chemical properties similar to the medium out of which it formed; and ‘second

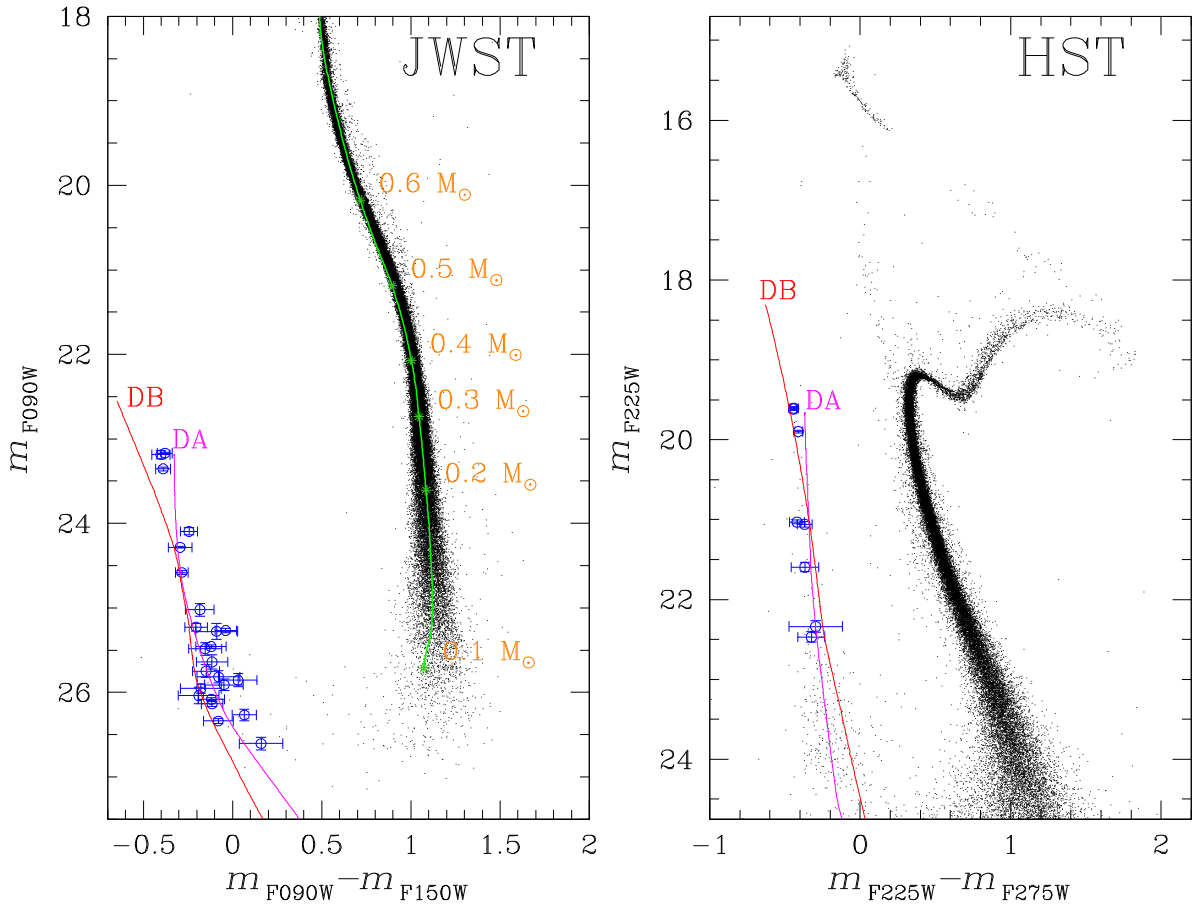


Figure 9. Comparison between IR *JWST* CMD (m_{F090W} versus $m_{F090W} - m_{F150W}$; left) and UV *HST* CMD (m_{F225W} versus $m_{F225W} - m_{F275W}$; right). The green line in the left-hand panel is the BASTI-IAC isochrone used to derive the photometric zero-point, with masses in steps of $0.1 M_{\odot}$ are indicated. In both CMDs, blue circles indicate the WDs identified in *JWST* data. Magenta and red lines delineate WD cooling tracks for hydrogen and helium envelopes, respectively.

generation’ populations (2Ps) which are enriched in helium and nitrogen, and depleted in carbon and oxygen, likely formed from the material processed by the 1P. Milone et al. (2018) found a maximum difference in helium between the 1P and 2Ps populations of $\delta Y_{\max} \sim 0.04$. Mészáros et al. (2015) reported average values of $[O/Fe] = 0.67$, $[C/Fe] = -0.42$, and $[N/Fe] = 0.89$ for 1P, and $[O/Fe] = 0.40$, $[C/Fe] = -0.38$, and $[N/Fe] = 1.03$ for 2Ps.

While a detailed analysis of the multiple population phenomenon is behind the scope of this work, we checked that the CMDs obtained with the *HST* UV/optical and *JWST* IR cross-matched catalogues. As shown by Salaris et al. (2019), the magnitudes of RGB and cool MS stars in the *JWST* filters contain signatures of CNO abundance variations typical of the multiple population phenomenon. Fig. 10 displays the m_{F150W} versus $m_{F275W} - m_{F150W}$ CMD, which shows a clear MS spread for $m_{F150W} \gtrsim 18.75$. We analysed in detail this spread to determine if it is due to photometric errors or the presence of multiple populations. We first verticalized the MS in the magnitude range $18.75 \leq m_{F150W} \leq 19.75$ calculating the 5th and 95th percentile of the colour distribution along the MS. We used these two fiducial lines (fid(5th) and fid(95th)) to calculate the quantity:

$$\Delta m_{F275W, F150W} = \frac{(m_{F275W} - m_{F150W}) - \text{fid}(95\text{th})}{\text{fid}(95\text{th}) - \text{fid}(5\text{th})}. \quad (2)$$

This verticalized MS is shown in Fig. 10, where the presence of multiple sequences is visually evident. We also discern multiple peaks in distributions of stars across the verticalized MS. We therefore

divided the CMD population into two parts: we assigned points with $\Delta m_{F275W, F150W} > -0.5$ to a group called PopA, and points with $\Delta m_{F275W, F150W} \leq -0.5$ to a group called PopB. PopA should contain the large part of 1P stars, so on average its photometric properties reflect 1P’s characteristics; while PopB tracks the (unresolved) 2Ps populations. We also evaluated the colour distributions of these two groups of stars in a sequence of CMDs of m_{F150W} versus $m_X - m_{F090W}$, with $X = F225W, F275W, F336W, F438W, F606W, F814W$, and $F150W$ (*HST* and *JWST* filters), i.e. using colours different from that used for the identification of the PopA/PopB groups in Fig. 10. We found that the two groups of stars form mostly separated sequences in each of these CMDs, differing in colour by up to 0.2 mag. The consistent separation of these groups strengthens the case that PopA and PopB stars belong to populations with different chemical properties.

6 SUMMARY

With the *James Webb Space Telescope* now fully operational, a new era of astronomy has begun. Its various instruments will allow us to observe not only the primordial Universe and exoplanet atmospheres, but also low-mass stars in globular clusters and resolved galaxies.

In this work, we have evaluated *JWST* data of the globular cluster M 92 collected with the NIRCам instrument for DD-ERS programme ERS-1334. We have used these data to derive a library of spatially varying effective PSFs for filters $F090W/F150W$ (SW)

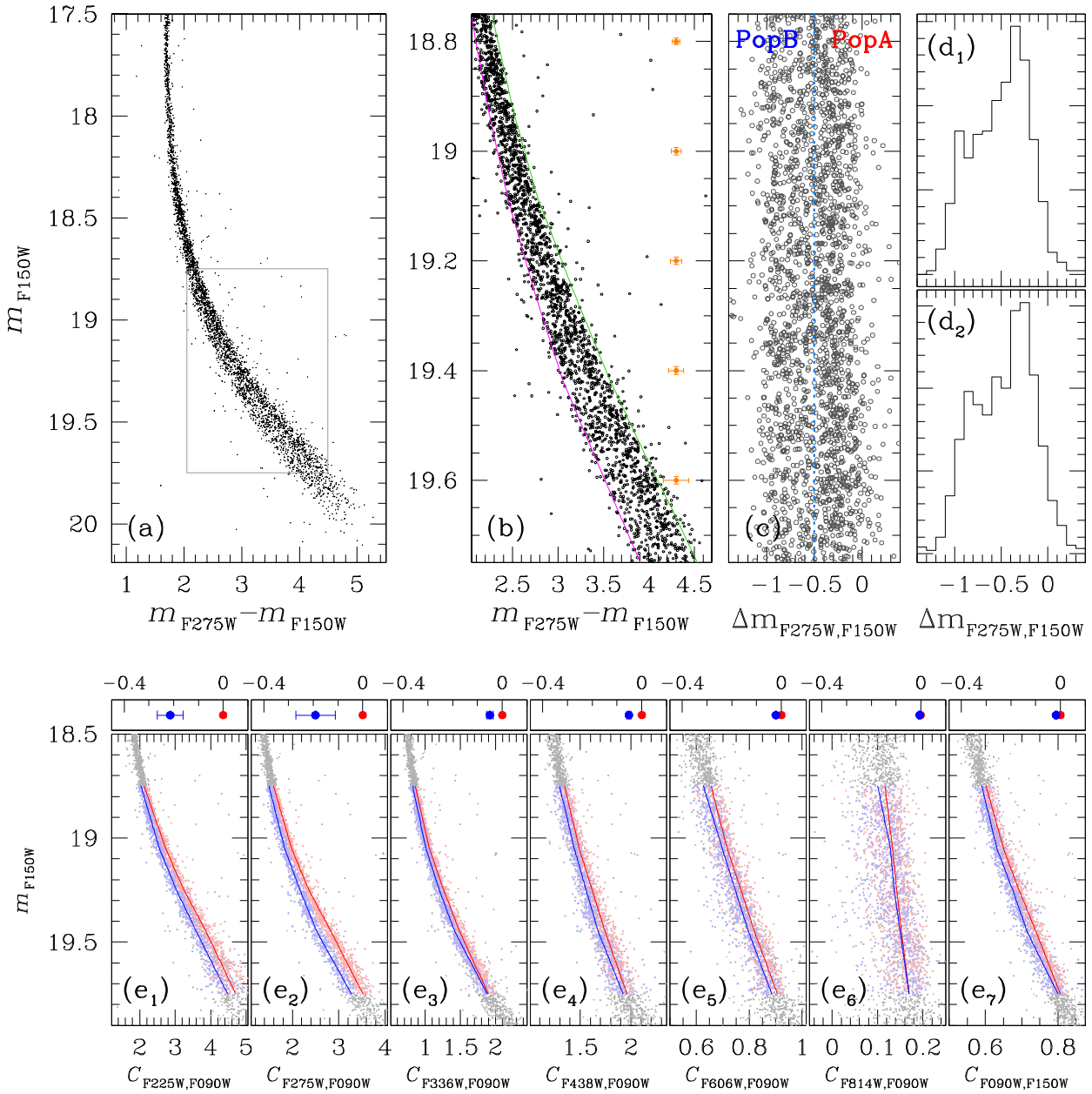


Figure 10. Multiple stellar populations discerned in the UV/optical/IR CMDs of M 92. Panel (a) shows the m_{F150W} versus $m_{F275W} - m_{F150W}$ CMD where the spread of the MS is evident for $m_{F150W} \gtrsim 18.75$. Panel (b) is a zoom of the MS for magnitudes $18.75 \leq m_{F150W} \leq 19.75$; magenta and green lines display the 5th- and 95th- percentile fiducial lines. Orange error bars along the right side of this panel indicate the photometric errors in intervals of 0.2 mag in $F150W$. Panel (c) shows the verticalized MS from panel (b). We are able to visually divide the stars in two groups: PopA (right) and PopB (left). Panels (d₁) and (d₂) show the distribution of sources across the verticalized MS in the magnitude ranges $18.75 \leq m_{F150W} < 19.25$ (panel (d₁)) and $19.25 \leq m_{F150W} < 19.75$ (panel (d₂)). Panels (e₁) through (e₇) show the colour distributions of PopA and PopB stars selected from the verticalized MS in the m_{F150W} versus $C_{X, F090W} = (m_X - m_{F090W})$ CMDs. Above each panel, the mean difference in colour between PopA (red) and PopB (blue) is indicated.

and $F277W/F444W$ (LW) for each of the individual detectors and modules. We have demonstrated that significant temporal variations are present in NIRCcam on the order of 3–4 percent based on a second set of observations of the Wolf–Lundmark–Melotte irregular galaxy obtained one month later under the same programme. We have also shown that these variations can be corrected by perturbing these library ePSFs, enabling high-precision photometry for various crowded regions over time. We have also demonstrated a method for calibrating instrumental magnitudes for individual NIRCcam detectors and filters using theoretical models and prior *HST* observations

of M 92, and provide measurements of the photometric zero-points for the individual detectors and filters used in this data set.

Our analysis allows for the first examination of *JWST* infrared CMDs for a globular cluster. We demonstrate that all of the CMDs are well-fit to theoretical 13 Gyr isochrones, and reach the lower bottom of M 92’s MS at a $S/N \sim 10$ –20 depending on the filter set. We also detect white dwarfs in the CMD in the $F090W$ and $F150W$ filters, and a cross-match of the *JWST* catalogues with the *HST* UV catalogue in $F225W$ and $F275W$ filters (obtained by us reducing data from GO-15173, PI: Kalirai) identifies 7 WDs in common.

The location of the WDs on the CMDs are also in agreement with theoretical $0.54 M_{\odot}$ WD cooling tracks.

We also searched for the presence of multiple stellar populations in the UV/IR CMD of the MS of M 92. We demonstrated that the m_{F150W} versus $(m_{F275W} - m_{F150W})$ CMD resolves a spread of the MS in the mass range of $0.5\text{--}0.6 M_{\odot}$ that is not attributable to photometric errors. Dividing the MS into two groups, PopA and PopB, corresponding approximately to 1P and 2P stars, respectively, we analysed the distributions of these populations in different combinations of colours. We found that the two groups almost always form two well-separated sequences, confirming that they are composed of stars with different physical and chemical properties.

ACKNOWLEDGEMENTS

The authors warmly thank the anonymous referee for carefully reading the paper and for the useful comments and suggestions that have contributed to improving the quality of the manuscript. The authors DN, LRB, MG, and MS acknowledge support by MIUR under PRIN program #2017Z2HSMF and by PRIN-INAF 2019 under program #10-Bedin. MS acknowledges support from The Science and Technology Facilities Council Consolidated Grant ST/V00087X/1. SC acknowledges financial support from ‘Progetto Premiale’ MIUR *MITIC* (PI: B. Garilli), progetto INAF Mainstream (PI: S. Cassisi) and from *PLATO* ASI-INAF agreement n.2015-019-R.1-2018, and from INFN (Iniziativa specifica TAsP). This work is based on observations made with the NASA/ESA/CSA James Webb Space Telescope. The data were obtained from the Mikulski Archive for Space Telescopes at the Space Telescope Science Institute, which is operated by the Association of Universities for Research in Astronomy, Inc., under NASA contract NAS 5-03127 for *JWST*. These observations are associated with program ERS-1334 (PI: Weisz). The authors acknowledge the ‘The *JWST* Early Release Science Program for Resolved Stellar Populations’ team led by D. Weisz, J. Anderson, M. L. Boyer, A. A. Cole, A. E. Dolphin, M. C. Geha, J. Kalirai, N. Kallivayalil, K. B. W. McQuinn, K. M. Sandstrom, B. F. Williams for developing their observing program with a zero-exclusive-access period. This research is also based on observations made with the NASA/ESA *Hubble Space Telescope* obtained from the Space Telescope Science Institute, which is operated by the Association of Universities for Research in Astronomy, Inc., under NASA contract NAS 5-26555. These observations are associated with programs GO-10775 (PI: Sarajedini), GO-13297 (PI: Piotto), and GO-15173 (PI: Kalirai).

DATA AVAILABILITY

The data underlying this article are publicly available in the Mikulski Archive for Space Telescopes at <https://mast.stsci.edu/>. The catalogues underlying this work are available in the online supplementary material of the article.

REFERENCES

Anderson J., 2016, Empirical Models for the WFC3/IR PSF, Instrument Science Report WFC3 2016-12. p. 42
 Anderson J., King I. R., 1999, *PASP*, 111, 1095
 Anderson J., King I. R., 2000, *PASP*, 112, 1360 (AK00)
 Anderson J., King I. R., 2004, Multi-filter PSFs and Distortion Corrections for the HRC, Instrument Science Report ACS 2004-15. p. 51

Anderson J., King I. R., 2006, PSFs, Photometry, and Astronomy for the ACS/WFC, Instrument Science Report ACS 2006-01. p. 34
 Anderson J., Bedin L. R., Piotto G., Yadav R. S., Bellini A., 2006, *A&A*, 454, 1029
 Anderson J. et al., 2008, *AJ*, 135, 2114
 Anderson J., Bourque M., Sahu K., Sabbit E., Viana A., 2015, A Study of the Time Variability of the PSF in F606W Images taken with the WFC3/UVIS, Instrument Science Report WFC3 2015-08. p. 19
 Bastian N., Lardo C., 2018, *ARA&A*, 56, 83
 Baumgardt H., Vasiliev E., 2021, *MNRAS*, 505, 5957
 Bellini A., Anderson J., Bedin L. R., 2011, *PASP*, 123, 622
 Borucki W. J. et al., 2010, *Science*, 327, 977
 Boyer M. L. et al., 2022, *RNAAS*, 6, 191
 Gaia Collaboration, 2016, *A&A*, 595, A1
 Gardner J. P. et al., 2006, *Space Sci. Rev.*, 123, 485
 Greene J. E. et al., 2019, *BAAS*, 51, 61
 Harris W. E., 1996, *AJ*, 112, 1487
 Hidalgo S. L. et al., 2018, *ApJ*, 856, 125
 Holmberg E., 1950, *MeLuS*, 128, 5
 Høg E. et al., 2000, *A&A*, 355, L27
 Jansen F. et al., 2001, *A&A*, 365, L1
 Kalirai J. S., Saul Davis D., Richer H. B., Bergeron P., Catelan M., Hansen B. M. S., Rich R. M., 2009, *ApJ*, 705, 408
 Larsen S. S., Brodie J. P., Grundahl F., Strader J., 2014, *ApJ*, 797, 15
 Libralato M., Bedin L. R., Nardiello D., Piotto G., 2016a, *MNRAS*, 456, 1137
 Libralato M. et al., 2016b, *MNRAS*, 463, 1780
 Lucertini F., Nardiello D., Piotto G., 2021, *A&A*, 646, A125
 Meixner M. et al., 2019, *BAAS*, 51, 554
 Melotte P. J., 1926, *MNRAS*, 86, 636
 Mészáros S. et al., 2015, *AJ*, 149, 153
 Milone A. P. et al., 2017, *MNRAS*, 464, 3636
 Milone A. P. et al., 2018, *MNRAS*, 481, 5098
 Nardiello D. et al., 2015, *MNRAS*, 451, 312
 Nardiello D., Libralato M., Bedin L. R., Piotto G., Borsato L., Granata V., Malavolta L., Nascimbeni V., 2016, *MNRAS*, 463, 1831
 Nardiello D. et al., 2018, *MNRAS*, 481, 3382
 Nardiello D., Piotto G., Milone A. P., Rich R. M., Cassisi S., Bedin L. R., Bellini A., Renzini A., 2019, *MNRAS*, 485, 3076
 Pietrinferni A. et al., 2021, *ApJ*, 908, 102
 Pilbratt G. L. et al., 2010, *A&A*, 518, L1
 Piotto G. et al., 2015, *AJ*, 149, 91
 Ricker G. R. et al., 2015, *J. Astron. Telesc. Instrum. Syst.*, 1, 014003
 Rieke M. et al., 2019, *BAAS*, 51, 45
 Salaris M., Cassisi S., Mucciarelli A., Nardiello D., 2019, *A&A*, 629, A40
 Salaris M., Cassisi S., Pietrinferni A., Hidalgo S., 2022, *MNRAS*, 509, 5197
 Sarajedini A. et al., 2007, *AJ*, 133, 1658
 Weisskopf M. C., Brinkman B., Canizares C., Garmire G., Murray S., Van Speybroeck L. P., 2002, *PASP*, 114, 1
 Werner M. W. et al., 2004, *ApJS*, 154, 1
 Windhorst R. et al., 2019, *BAAS*, 51, 449
 Wolf M., 1909, *Astron. Nachr.*, 183, 187
 Wright E. L. et al., 2010, *AJ*, 140, 1868

SUPPORTING INFORMATION

Supplementary data are available at *MNRAS* online.

supplementary.data

Please note: Oxford University Press is not responsible for the content or functionality of any supporting materials supplied by the authors. Any queries (other than missing material) should be directed to the corresponding author for the article.

APPENDIX A: WHITE DWARFS ON THE STACKED IMAGE

In Fig. A1 we show three WDs on the three-colour stacked image ($F090W + F150W + F444W$), to demonstrate that they are point sources. The first two WDs from the left have magnitude $m_{F090W} \sim 23.2$, the last have magnitude $m_{F090W} \sim 25.8$.

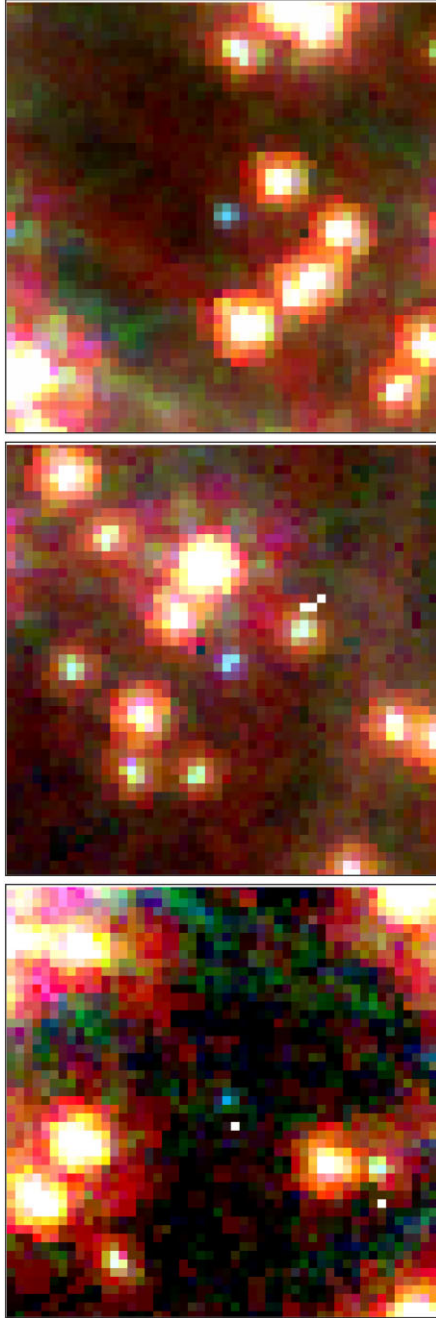


Figure A1. Three white dwarfs on the colour-stacked image.

APPENDIX B: ELECTRONIC MATERIAL

The catalogues obtained in this work will be available electronically as supporting material to this paper. We will release a catalogue for each detector and for each filter (totally 20 catalogues). A description of the columns of the catalogues is reported in Table B1. We will also release the PSF arrays on the website https://web.oapd.inaf.it/b edin/files/PAPERS_eMATERIALs/JWST/Paper_01/.

Table B1. Description of the columns of the released catalogues.

Column	Name	Unit	Explanation
01	X	pixel	X stellar position in the reference system of the detector
02	Y	pixel	Y stellar position in the reference system of the detector
03	MAG		Calibrated VEGAMAG magnitude
04	SIGMA_MAG		Photometric error
05	QFIT		Quality-fit parameter

Note. The name of each file reports the information on the catalogue: NGC6341.JWST.X.YZ.CAT, where X = F090W, F150W, F277W, F444W is the filter, Y = A, B is the module, and (only for SW channel) Z = 1,2,3,4 is the detector number.

This paper has been typeset from a $\mathrm{T}_{\mathrm{E}}\mathrm{X}/\mathrm{L}^{\mathrm{A}}\mathrm{T}_{\mathrm{E}}\mathrm{X}$ file prepared by the author.